Engineering xxx (xxxx) xxx

Contents lists available at ScienceDirect

Engineering

journal homepage: www.elsevier.com/locate/eng

Research
Organoids and Organs-on-Chips—Feature Article

Construction of Multicellular Tumor-On-A-Chip Models for Ovarian Cancer Research

Jiexian Ye [a,c,#], Hao Lin [b,#], Zilin Zhang [a], Shihui Xu [a,c,d], Feili Yang [c], Xuemei Zhuansun [c], Feng Ji [b], Yusha Zhang [e], Yuxin Zhu [e], Jing Zhang [c], Zaozao Chen [a,c,*], Zhongze Gu [a,c,*], Yang Shen [e,**]

[a] State Key Laboratory of Digital Medical Engineering, School of Biological Science and Medical Engineering, Southeast University, Nanjing 210096, China
[b] Department of Clinical Science and Research, Zhongda Hospital, School of Medicine, Southeast University, Nanjing 210009, China
[c] Jiangsu Avatarget Biotechnology Co., Ltd., Suzhou 215163, China
[d] Institute of Medical Devices (Suzhou), Southeast University, Suzhou 215163, China
[e] Department of Obstetrics and Gynaecology, Zhongda Hospital, School of Medicine, Southeast University, Nanjing 210009, China

ARTICLE INFO

Article history:
Received 29 December 2024
Revised 14 August 2025
Accepted 18 August 2025

Keywords:
Ovarian cancer
Chimeric antigen receptor-mesothelin-T
Organoid
Tumor-on-a-chip
Tumor microenvironment

ABSTRACT

Ovarian cancer remains a highly lethal gynecologic malignancy. Early diagnosis poses significant challenges, and the five-year survival rate is consistently below 45 %. Current standard-of-care combines surgical resection with platinum-based chemotherapy. Emerging therapeutic modalities like chimeric antigen receptor-T (CAR-T) therapy show promise, though they face efficacy constraints due to tumor heterogeneity and immunosuppressive microenvironments. Conventional models including two-dimensional (2D) cultures and patient-derived xenografts are increasingly supplanted by organoid and tumor-on-a-chip technologies due to intrinsic limitations and poor clinical translatability. This study established multiple tumor-on-a-chip platforms derived from ovarian cancer organoids and conducted systematic *in vitro* drug sensitivity screening. Furthermore, by utilizing patient-derived organoids to engineer multicellular dynamic microenvironments, we achieved one of the extremely limited evaluations of CAR-T efficacy against solid tumors within ovarian cancer microfluidic systems. This work establishes an enhanced preclinical platform to advance therapeutic screening and personalized treatment development.

1. Introduction

Ovarian cancer constitutes a leading malignant tumor in the female reproductive system, characterized by high incidence and mortality rates [1]. Its subtle early symptoms mean approximately 75 % of patients are diagnosed at an advanced stage, resulting in a five-year survival rate of merely 30 % [2]. Primary management involves surgical resection and chemotherapy, though emerging therapies like molecular-targeted agents and chimeric antigen receptor-T (CAR-T) show promise [3]. Significant treatment hurdles include high tumor heterogeneity and complex microenvironmental dynamics.

Current preclinical ovarian cancer models encompass tumor cell lines, animal models, spheroids, organoids, and tumor-on-chips [4–9]. Cell lines are simple to culture but poorly to replicate tumor heterogeneity. Animal models preserve key tumor characteristics but are costly and time-intensive to establish. As newer platforms, organoids and tumor-on-chips better retain tumor complexity and mimic microenvironments, showing strong developmental potential [10–15]. Nevertheless, research on ovarian cancer organoids—particularly tumor-on-chip systems—remains disproportionately scarce compared to other malignancies, necessitating exploratory investigations in this domain.

Current research primarily focuses on organoid cultivation [16–18] and cell line-based complex models, ignoring critical gaps in sophisticated ovarian cancer organoids-derived *in vitro* systems [19]. Joy et al. [20] developed a three-dimensional (3D) ovarian cancer model incorporating spheroids, ovarian cancer-associated

* Corresponding author at: State Key Laboratory of Digital Medical Engineering, School of Biological Science and Medical Engineering, Southeast University, Nanjing 210096, China.
** Corresponding author.
E-mail addresses: zaozaochen@seu.edu.cn (Z. Chen), gu@seu.edu.cn (Z. Gu), shenyang@seu.edu.cn (Y. Shen).
# These authors contributed equally to this work.

https://doi.org/10.1016/j.eng.2025.08.028

Please cite this article as: J. Ye, H. Lin, Z. Zhang et al., Construction of Multicellular Tumor-On-A-Chip Models for Ovarian Cancer Research, Engineering, https://doi.org/10.1016/j.eng.2025.08.028

fibroblasts (CAFs), and vascular components, represents current progress. However, this model relies on cell line-derived spheroids, limiting its heterogeneity replication. Lal-Nag et al. [21] established a 3D model combining human ovarian cancer cell with primary mesothelial cells and fibroblasts. Although using 3D architecture, this system fails to replicate tumor properties and lacks dynamic biophysical microenvironments. Ibrahim et al. [22] created a dynamically cultured complex model using three ovarian cancer cell lines with endothelial cells, adipocytes, and mesothelial cells, yet omitted tumor-associated fibroblasts and exhibited complex construction protocols limiting high-throughput applications. Dadgar et al.'s microfluidic platform [23] facilitates efficient spheroid formation but prioritizes technical engineering over biological relevance including cellular provenance, microenvironmental composition, and vascular architecture. Collectively, existing *in vitro* models demand critical improvements despite increasing scientific interest.

In this study, we successfully constructed ovarian cancer organoids and spheroids, validated their consistency with the original tumors, and developed two types of ovarian cancer chips, offering novel tools for drug screening and personalized therapy. These models revealed the significant impact of tumor heterogeneity and the microenvironment on therapeutic efficacy. We further evaluated and analyzed the performance of chemotherapeutic agents and CAR-T cell therapies using these platforms.

2. Materials and methods

2.1. Isolation of ovarian cancer organoids and CAFs

This study was conducted in accordance with the *Declaration of Helsinki* and approved by the Ethics Committee of Zhongda Hospital Affiliated to Southeast University.

Fresh tissue samples were washed, minced into small fragments, and digested using 3 mL collagenase (1 $mg{\cdot}mL^{-1}$; C9407; Sigma-Aldrich, USA) at 37 °C for 30–60 min until dissociation into single cells. Digestion was terminated by adding 10 mL phosphate-buffered saline (PBS). The cell suspension was filtered through a 100 μm cell strainer (352360; Falcon, USA), and the filtrate centrifuged at 1000 $r{\cdot}min^{-1}$ for 5 min at room temperature. Pelleted cells were resuspended in Matrigel, mixed thoroughly, and plated onto 24-well plates at approximately 30 μL per well. After Matrigel solidification, 500 μL organoid medium was added per well, followed by incubation at 37 °C with 5 % CO_2. Medium was replaced every 2–3 d, with growth changes documented photographically.

The extraction protocol for ovarian CAFs is identical to the organoid methodology, requiring only substitution of the culture medium with fibroblast-specific medium.

2.2. Organoid and cell culture

Ovarian cancer organoids were grown in Dulbecco's modified Eagle's medium (DMEM)/F12 (11320-033; Gibco, USA) containing 50 $ng{\cdot}mL^{-1}$ Noggin (HY-P7051A; MCE, USA), 50 $ng{\cdot}mL^{-1}$ RSPO1 (HY-P7114; MCE), 1.25 $nmol{\cdot}L^{-1}$ *N*-acetylcysteine (HY-B0215; MCE), 1 × B27 (17504-044; Gibco), 10 $mmol{\cdot}L^{-1}$ nicotinamide (N0636; Sigma-Aldrich), 500 $nmol{\cdot}L^{-1}$ A83-01 (HY-10432; MCE), 10 $ng{\cdot}mL^{-1}$ fibroblast growth factor 10 (FGF10; HY-P7342AF; MCE), 5 $ng{\cdot}mL^{-1}$ epidermal growth factor (EGF; AF-100-15-500UG; PeproTech, USA), 37.5 $ng{\cdot}mL^{-1}$ heregulin β-1 (100-03-50UG; PeproTech), 5 $\mu mol{\cdot}L^{-1}$ Y27632 (HY-10071; MCE), 10 $\mu mol{\cdot}L^{-1}$ forskolin (HY-15371; MCE), 500 $ng{\cdot}mL^{-1}$ hydrocortisone (HY-N0383; MCE), 100 $ng{\cdot}mL^{-1}$ β-estradiol (HY-B0141; MCE), 100 $mg{\cdot}mL^{-1}$ primocin (ant-pm-1; Invivogen, France), 1 % penicillin/streptomycin (15140-122; Gibco). Ovarian CAFs were grown in human fibroblast-serum-free medium (AC-1001015; Applied Cell, China). Human umbilical vein endothelial cells (HUVECs) were cultured in endothelial cell medium (ECM; 1001; Sciencell, USA). T cells and chimeric antigen receptor (CAR)-mesothelin (MSLN)-T cells were cultured in X-VIVO® 15 medium (0001333753; Lonza, USA) containing 100 $IU{\cdot}mL^{-1}$ interleukin-2 (IL-2; 589104; Bioledend, USA).

All organoids and cells were cultured in a 5 % CO_2 atmosphere at 37 °C and both medium were changed every 2–3 d.

2.3. Ovarian cancer spheroids construction

Ovarian cancer organoids were dissociated into single cells using trypsin (15050065; Gibco). CAFs were pretreated with 1 $\mu g{\cdot}mL^{-1}$ mitomycin C for 6 h prior to TrypLE (12605028; Gibco) mediated single-cell dissociation. HUVECs were digested to single-cell suspension with TrypLE.

The single-cell suspensions of ovarian cancer organoids, CAFs, and HUVECs were mixed at a 5:5:1 ratio [24], and 200 μL aliquots were transferred to anti-adhesion-treated 96-well U-bottom plates. Following centrifugation at 400*g* for 5 min at room temperature, the plates were incubated at 37 °C with 5 % CO_2.

Spheroid formation was observed after approximately 18 h of culture. By 48 h, spheroids exhibited increased density and structural stability. Based on experimental requirements, spheroids were subsequently transferred to culture plates/chips and embedded in Matrigel for subsequent culture.

2.4. Cell tracker of ovarian cancer spheroids

Following single-cell dissociation of ovarian cancer organoids, CAFs, and HUVECs, distinct cell tracker fluorescent probes were applied: green for organoids (C2925; Thermo Fisher Scientific, USA), blue for CAFs (C2110; Thermo Fisher Scientific), and red for HUVECs (C34552; Thermo Fisher Scientific). After 30 min incubation at 37 °C, cells were washed twice with PBS. The three cell suspensions were proportionally mixed, and 200 μL aliquots were transferred to anti-adhesion-treated 96-well U-bottom plates. Following centrifugation at 400*g* for 5 min, cellular distribution was examined using fluorescence microscopy.

2.5. Construction of ovarian cancer spheroid model using high-throughput microfluidic chips

First, ovarian cancer spheroids were constructed. Once the structure became dense and stabilized, the spheroids were aspirated with a 10 μL pipette, transferred to the central well of the small unit of the high-throughput microfluidic chips, and enough Matrigel was added for 3D incubation. After the Matrigel solidified, medium was added to each of the three wells in the small unit. Next, the microfluidic chips were transferred to the swinging perfusion apparatus for dynamic incubation. The incubation was set to a shaking angle of 7° and a shaking time of 8 min [25].

2.6. Construction of multicellular ovarian cancer model using plug-in microfluidic chips

Firstly, ovarian cancer spheroids were constructed, and ovarian CAFs were pretreated for 6 h with mitomycin C (1 $\mu g{\cdot}mL^{-1}$, HY-13316; MCE). HUVECs were digested into single cells using TrypLE, adjusted to a cell density of 4×10^5 $cells{\cdot}mL^{-1}$, and inoculated onto the underside of a Transwell membrane. The endothelial cells were allowed to adhere for 2 h. Subsequently, the Transwell was transferred to a plug-in chip, and endothelial cell culture medium (500 μL) was added to the lower chamber.

The pretreated ovarian CAFs were also digested into single cells using TrypLE, adjusted to the same cell density (4×10^5 cells·mL^{-1}), and CAFs suspension (50 μL) was inoculated into each well. After 2 h, medium (500 μL) was added to the upper chamber. The medium in the Transwell's upper chamber was aspirated, and ovarian cancer spheroids were transferred into the Transwell, supplemented with mixed medium (500 μL). The chip was then placed in an incubator and cultured statically for 24 h, allowing the spheroids to adhere tightly to the CAF layer.

Prior to immune cell introduction, the vascular endothelial layer was pre-stimulated with 2 ng·mL^{-1} tumor necrosis factor-α (TNF-α; H8916; Sigma-Aldrich) for 2 h. All medium in the chip was aspirated and discarded, and immune cell was added to the lower chamber of the Transwell, with cell medium (300 μL) added to the upper chamber. The chip was then placed on a shaking perfusion device for dynamic culture, set to a shaking angle of 7° and a shaking duration of 8 min [25].

2.7. Assessment of CAR-MSLN-T therapy using ovarian cancer chips

Preliminary assessment experiment: 5000 T/CAR-MSLN-T cells and 5 μL caspase3 apoptosis detection reagent (C10777S; Beyotime, China) were added to the lower chamber per chip unit. Fluorescence imaging was performed at 4, 24, and 48 h, followed by statistical analysis of apoptotic signal intensity using ImageJ.

Colocalization analysis experiment: 5000 Cell Tracker™ Red-labeled T/CAR-MSLN-T cells (C34552; Thermo Fisher Scientific) and 5 μL caspase3 (C10777S; Beyotime) apoptosis detection reagent were added to the lower chamber per chip unit. Confocal imaging was conducted after 24 h, succeeded by spots reconstruction and colocalization analysis.

Viability assay experiment: Each chip unit was added with 5000 T/CAR-MSLN-T cells. Following 48 h incubation, quantitative analysis of cell viability was performed using the CellTiter-Glo® 3D Assay Kit (Cat. G9683; Promega, USA).

2.8. Hematoxylin and eosin (H&E) staining

Ovarian cancer tissues, organoids, and spheroids samples were stained using a H&E staining kit (C0105S; Beyotime). Following fixation with 4 % paraformaldehyde (PFA; BL539A; Biosharp, China), samples underwent dehydration, clearing, paraffin embedding, and sectioning. Sections were baked at 60 °C for 30–60 min, sequentially treated with xylene and absolute ethanol, then rehydrated through graded ethanol series, rinsed with water, and washed with PBS.

Sections were stained with hematoxylin for 3–8 min, differentiated in acid-alcohol, counterstained with eosin for 1 min, dehydrated through reverse-graded ethanol, cleared in xylene, and mounted with neutral resin. Slides were air-dried and stored at ambient temperature.

2.9. Immunohistochemistry (IHC)

Immunohistochemical staining was performed on ovarian cancer tissues, organoids, and spheroids samples. Paraffin-embedded sections from 4 % PFA specimens underwent baking at 60 °C for 30 min, deparaffinization in xylene, and graded ethanol hydration. Following microwave-mediated antigen retrieval using high power until boiling then low power for 10 min with subsequent natural cooling, sections were blocked with blocking buffer (P0260; Beyotime) for 30 min. Primary antibodies were incubated overnight. After PBS washes, secondary antibody incubation proceeded at room temperature for 30 min. A 3,3′-diaminobenzidine (DAB) kit (P0202; Beyotime) was used for chromogenic development, which was monitored microscopically. Hematoxylin counterstaining lasted 2 min followed by acid-alcohol differentiation. Sections were dehydrated through increasing ethanol concentrations, cleared in xylene, and permanently mounted with neutral balsam under coverslips.

2.10. Immunofluorescence staining

Immunofluorescence was employed to detect α-smooth muscle actin (α-SMA) expression in ovarian CAFs and MSLN expression in ovarian cancer spheroids. Samples were fixed with 4 % PFA, permeabilized with 0.3 % Triton X-100 (P0096; Beyotime) at room temperature for 10–30 min, and blocked with immunostaining blocking buffer (P0260; Beyotime) for 30–60 min. Without washing, primary antibodies (a-SMA; ab7817, 1:200 diluted; Abcam, UK; MSLN; ab309516, 1:100 diluted; Abcam) were directly applied and incubated overnight. After PBS washes, secondary antibodies (488-conjugated goat anti-mouse immunoglobulin G (IgG); A-11029; Invitrogen, USA; 594-conjugated donkey anti-rabbit IgG; 711–585-152, 1:1000 diluted; Jackson, USA) were added for light-protected incubation for 1 h. Following additional PBS washes, nuclei were counterstained with 4′,6-diamidino-2-pheny lindole (DAPI; R37606; Invitrogen) for 5 min under light protection. Imaging was performed using fluorescence microscopy after final washing.

2.11. Live/dead staining

Cellular viability within drug-exposed spheroids was assessed using a live/dead assay. Culture medium was discarded from the microplate wells and replaced with 200 μL of pre-formulated live/dead staining reagent (R37601; Invitrogen). The plate was incubated at 37 °C for 30 min, followed by fluorescence imaging at 488 nm and 570 nm excitation wavelengths. Viable cells exhibited green fluorescence whereas dead cells displayed red fluorescence.

2.12. Cell viability assay

Cellular viability following drug sensitivity testing and CAR-T therapy was assessed using the CellTiter-Glo® 3D Assay Kit. For post-treatment, an equal volume of CellTiter-Glo® 3D reagent relative to culture medium was added to either multiwell plates or chip chambers. The samples were vigorously mixed on an orbital shaker for 5 min, incubated at room temperature under light protection for 25 min, transferred to opaque-walled microplates, and luminescence signals quantified using a multifunctional microplate reader.

2.13. Whole exome enqueueing data analysis

Agilent SureSelect Human Al ExonV6 Capture Kit (Agilent Technologies, USA) was used to capture the whole exome regions for whole exome sequencing (WES). The DNA libraries were sequenced on the NovaSeq 6000 platform (Illumina, USA) to generate 150 bp paired-end reads at Nanjing Jiangbei New Area Biopharmaceutical Public Service Platform Co., Ltd. (China).

Sequence reads were subsequently aligned to the human reference genome GRCh37(hg19) using Burrows-Wheeler Aligner (v0.7.17). The mapped data were further processed for quality control and mutation calling using the Genome Analysis Toolkit (GATK; v4.2.5.0) based on its best practices workflows. The final somatic variants were annotated using the Annovar. Copy number alterations (CNAs) was analyzed by copy number variation (CNV) kit (v0.9.9). Mutational signatures were analyzed using the Mutational Patterns R package (v3.4.1).

2.14. RNA-sequencing (RNA-seq) data analysis

Total RNA was isolated from samples using the RNAiso Plus Kit (Takara, China) following the manufacturer's protocol. RNA concentration and integrity were assessed using a Qubit 4.0 Fluorometer (Thermo Fisher Scientific) and an Agilent 2100 Bioanalyzer (Agilent Technologies), respectively. RNA-seq libraries were constructed with the VAHTS Stranded messenger RNA sequencing (mRNA-seq) Library Prep Kit for Illumina (Vazyme Biotech, China). Sequencing was performed on an Illumina NovaSeq 6000 platform with 150 bp paired-end reads. Raw sequencing reads were subjected to quality control using Fastp (v0.23.2) to remove low-quality sequences and adapter contamination. High-quality reads were aligned to the GRCh38 human reference genome via HISAT2 (v2.2.1). Transcript assembly and quantification were conducted using StringTie (v2.2.1), followed by normalization of expression data with the DEGseq R package (v1.48.0) for differential expression analysis.

2.15. Statistical analysis

Statistical tests were performed and statistical plots were drawn using GraphPad Prism version 6.0 software, and the results are expressed as mean ± standard error of mean (SEM), with no statistically significant differences, $p > 0.05$, shown as ns; data for indicators of statistical significance are: $^{*}p < 0.05$, $^{**}p < 0.01$, $^{***}p < 0.001$, $^{****}p < 0.0001$.

3. Results

3.1. Ovarian cancer organoid construction and characterization

Primary ovarian cancer surgical specimens were processed to generate organoids. A portion of primary ovarian cancer surgical specimens was reserved for sequencing and characterization. The remaining specimens were washed, mechanically dissociated, enzymatically digested, and filtered to obtain single cells or small cell clusters, followed by embedding in Matrigel for 3D culture (Fig. 1(a)). We established ovarian cancer organoids encompassing multiple subtypes, including high-grade serous carcinoma (HGSC), borderline tumors (BTs), mucinous adenocarcinoma (MA), clear cell carcinoma (CCC), endometrioid carcinoma (END), and invasive transitional cell carcinoma (IT). Ovarian cancer organoids displayed broad morphological diversity as shown in Fig. 1(b) [26]. Most HGSC organoids were densely solid with size heterogeneity; HGSC-1, -2, and -4 had diffuse boundaries whereas HGSC-5 showed unique thin-walled cystic architecture. The BT organoids all displayed regular cystic morphology, with a larger size, faster growth rate, and higher proliferation efficiency compared to other pathological types. The morphology of MA organoids varied significantly, demonstrating superior size expansion kinetics and proliferative capacity versus other subtypes. CCC-1 produced grapevine-like clusters of thin-walled cell. END-1 and IT-1 displayed solid irregular spheroids. Collectively, organoids recapitulated tumor heterogeneity.

Immunohistochemical staining of two HGSC organoids, one BT organoid, and one MA organoid confirmed phenotype retention (Fig. 1(c)). HGSC-1 showed concordant high tumor proliferation marker Ki67 in tumor/organoid, overexpressed p53, and estrogen receptor $(ER)^{+}$ status. HGSC-4 maintained $Ki67^{+}/ER^{+}/p53^{-}$ expression patterns in both. BT-1 preserved $Ki67^{+}/ER^{+}/p53^{+}$ profiles. MA-1 retained primary tumor phenotypes, validating mutational landscape conservation [27–29].

The morphological structures of organoids from different pathological types varied, as shown in Fig. 1(d). All organoids reproduced tumor hallmarks including hobnail cells, papillary structures, and nuclear atypia observed in matched tissues, confirming intratumoral heterogeneity retention [26–29].

3.2. Gene sequencing analysis of ovarian cancer samples and their derived organoids

Building on the histopathological concordance, we genomically validated the genetic similarity between ovarian cancer organoids and their corresponding primary tumor samples from a genomic perspective. WES was performed on BT-1, MA-1, HGSC-7, HGSC-8, and their parental tumors.

Ovarian cancer faithfully preserved CNV observed in the whole exome of the primary tumor samples, although some exhibited amplified CNVs (Fig. 2(a)). Concurrent concordance of multiple mutation loci (Fig. 2(b)), similarity of single nucleotide polymorphisms (SNPs) (Fig. 2(c)), and high-level consistency of insertion–deletion mutations (INDELs) (Fig. 2(d)) were observed. Fig. S1 in Appendix A illustrates the somatic mutational concordance between ovarian cancer organoids and the corresponding tumor tissues. The characteristically observed B-Raf proto-oncogene (*BRAF*) mutation in BT-1 modulates proliferation/differentiation [30]. Tumor protein P53 gene (*TP53*) mutations, frequently observed in 96 % of HGSC subtypes, were present in both HGSC-7 and HGSC-8 samples [31]. These mutations impair p53 protein function, which is crucial for DNA damage response, repair, cell cycle regulation, and apoptosis, are found in majority of cancers. Additionally, HGSC-8 harbors a breast cancer 1 gene (*BRCA1*) mutation, which disrupts DNA double-strand break repair and increases genomic instability. MA-1 exhibits *TP53*/neurofibromatosis type 1 gene (*NF1*) mutations promoting tumorigenesis [32], though unverifiable due to lacking primary tumor sequencing data.

Genetic similarity indices were 93 % (BT-1), 87 % (MA-1), 79 % (HGSC-7), and 83 % (HGSC-8). Aggregate similarity reached 85.5 %, confirming high genomic fidelity of organoids to original tumors.

3.3. Construction and characterization of drug-sensitive tumor chips for ovarian cancer research

To investigate the growth rate of different organoid samples, we longitudinally monitored and quantified ovarian cancer spheroid development. The radius, area, perimeter, and other parameters of the spheroids were measured using artificial intelligence (AI)-based automatic analysis (Figs. 3(a) and (b)). On day 0, ovarian cancer organoids, vascular endothelial cells, and ovarian CAFs were collected at the bottom of the U-plate via centrifugation. Spheroid initiation commenced on day 1, with progressive densification observed by day 2. By day 3, the spheroids were more compact and their structure gradually stabilized. From day 4 to day 8, the spheroids were transferred to Matrigel for further culture, during which the spheroid structure underwent sustained densification and stabilization. Initial structural maturation correlated with transient radius/area reduction, whereas subsequent culture in Matrigel induced steady dimensional expansion (radius/area increase).

Cell tracker staining confirmed homogeneous cellular distribution (organoids-green, endothelial-red, CAFs-blue; Fig. 3(c)). H&E/IHC demonstrated positive Pan cytokeratin (Pan-CK), α-SMA, and CD31 expression, indicating robust viability. Spheroids exhibited solid tumor morphology with endothelial-derived vasculature-like structures (Fig. 3(d)).

For ovarian cancer drug sensitivity assessment, spheroids were primarily assembled in 96-well U-plates followed by transfer to microfluidic chips and dynamic perfusion culture on a shaking perfusion apparatus (Fig. 3(e)). The structure of the microfluidic chip used in this model is shown in Fig. 3(f). High-throughput microflu-

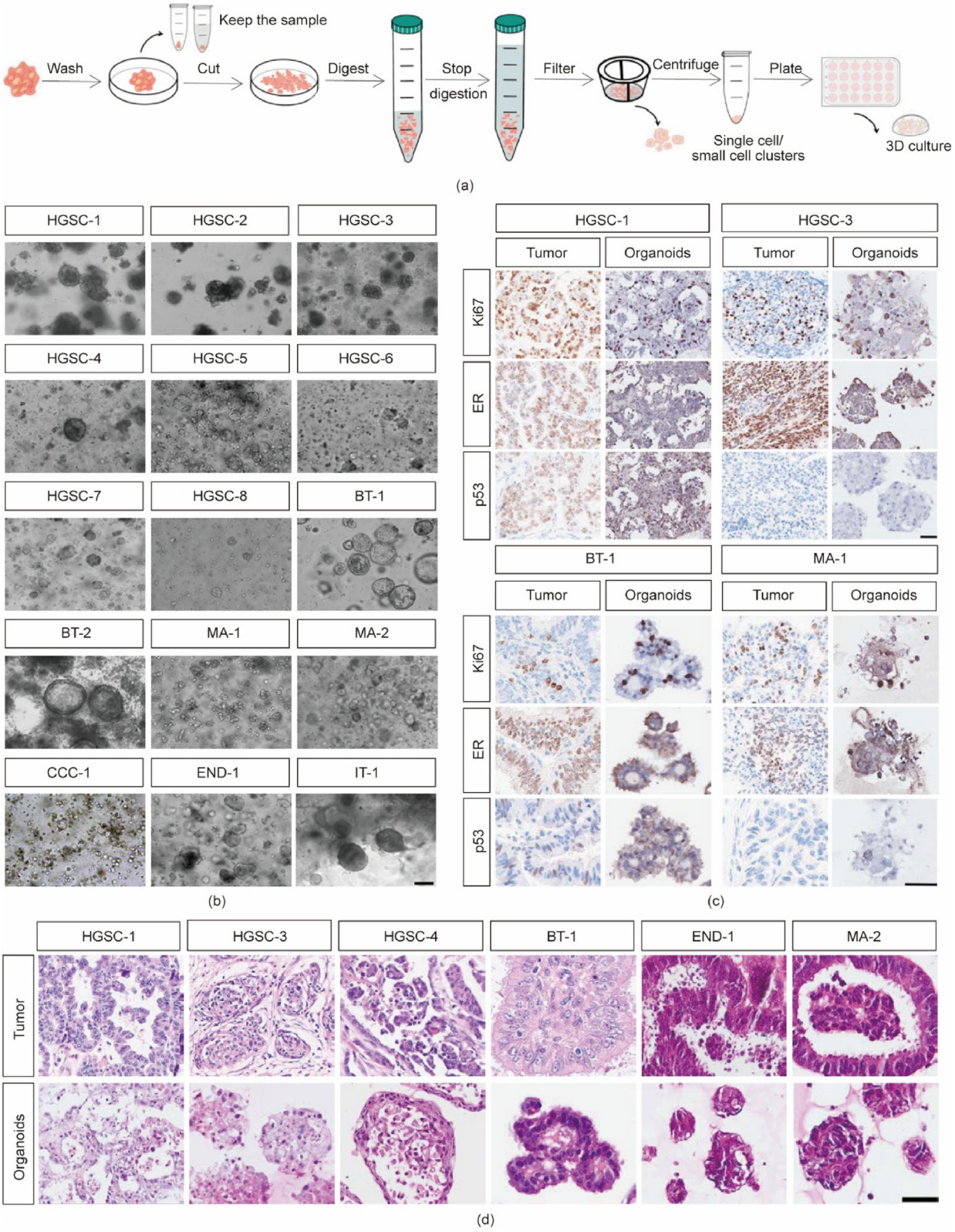

Fig. 1. Ovarian cancer organoid construction and characterization. (a) Primary ovarian cancer sample extraction process. (b) Brightfield image of ovarian cancer organoids. Scale bar: 300 μm. (c) Immunohistochemical staining of ovarian cancer tumor tissues and organoids. Scale bars: 50 μm. (d) H&E staining of ovarian cancer tumor tissue and organoids. Scale bar: 50 μm. ER: estrogen receptor.

idic chips consists of 128 units with tripartite microchambers interconnected via bottom microchannels, enabling high-throughput screening. Comparative morphometric analysis in Figs. 3(g)–(i) revealed time-dependent increases in both radius and area, where microfluidic dynamic culture significantly enhanced growth rates relative to static conditions.

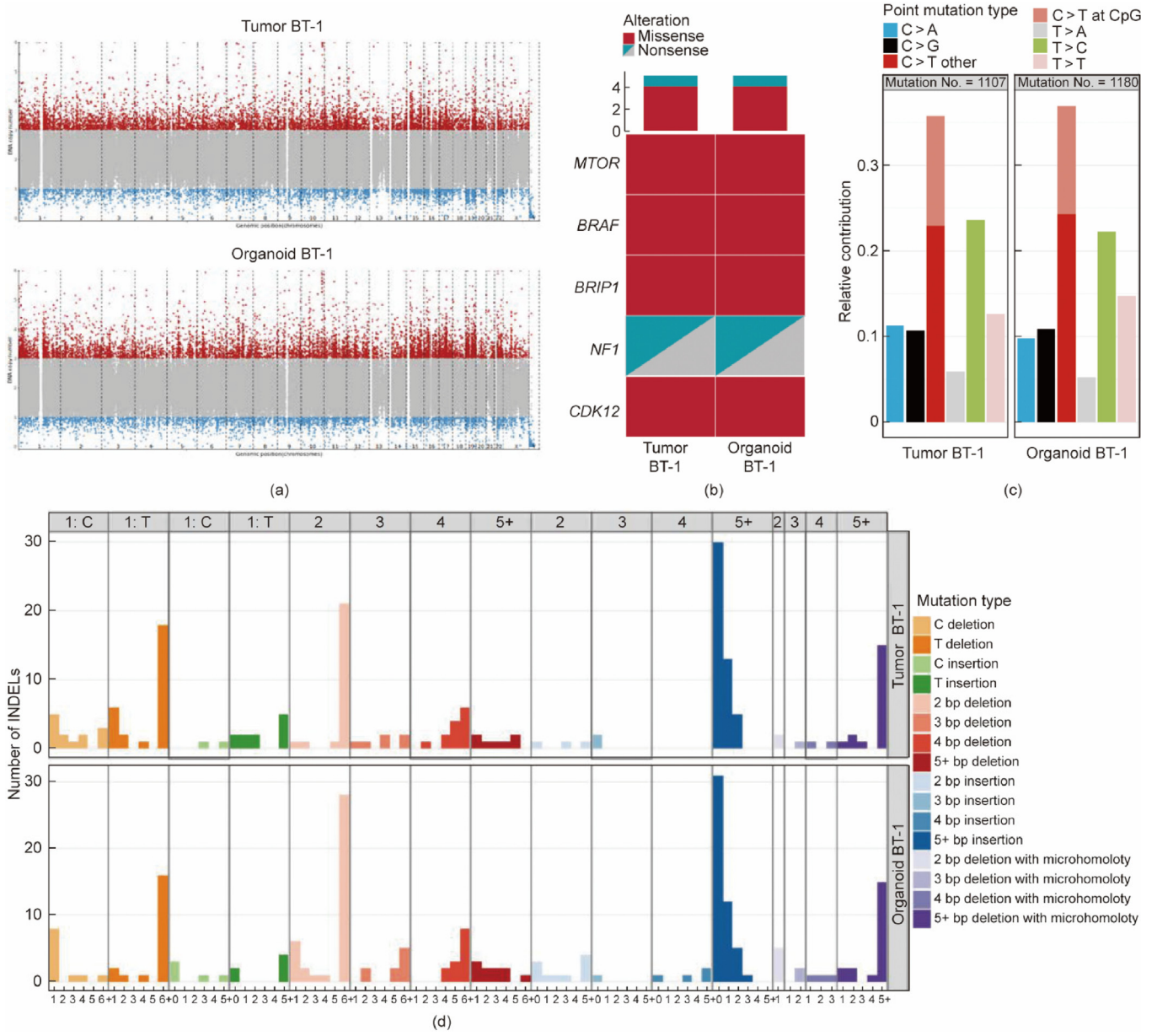

Fig. 2. Gene sequencing analysis of ovarian cancer sample BT -1 and its derived organoids. (a) CNV. (b) Expression of key gene loci. (c) SNP mutation characteristics. (d) INDEL mutation characteristics.

3.4. High-content analysis of ovarian cancer models

We performed quantitative high-content analysis of ovarian cancer organoid and spheroid growth dynamics in Fig. 4 using semi-automated imaging (automated recognition with manual correction), extracting multiparametric metrics including: growth kinetics (area, diameter/radius, perimeter), morphology (roundness, aspect ratio, opacity), and invasion potential via the excess perimeter index (EPI = actual perimeter/equivalent circular perimeter) to quantify peripheral protrusion complexity [33].

Analysis of ten organoid trajectories (Figs. 4(a)–(c)) revealed nine day expansion from 56 203.11 to 227 331.11 μm^2 (304.48 % area increase) and 2835.58 to 5135.92 μm perimeter (81.12 % growth), confirming robust proliferation. High-content analysis derived multiple parameters: radius, area, and perimeter measurements confirmed rapid organoid proliferation, while aspect ratio and roundness analyses indicated sustained near-circular morphology throughout culture. EPI assessment further revealed progressive invasiveness reduction (Fig. 4(c)).

Similarly, on-chip analysis of ovarian cancer spheroids captured seven key parameters—area, perimeter, radius, roundness, width height ratio, opacity, and EPI. Comparative analysis (Figs. 4(d) and (e)) demonstrated that dynamic perfusion significantly accelerated time-dependent expansion versus static environments. Analysis revealed no significant variations in spheroid roundness, width height ratio, or opacity across diverse culture conditions or growth durations. However, spheroid EPI—an invasiveness indicator [33]—exhibited distinct patterns: under static conditions, redundant perimeter gradually increased (suggesting escalating invasiveness), whereas dynamic conditions showed initial redun-

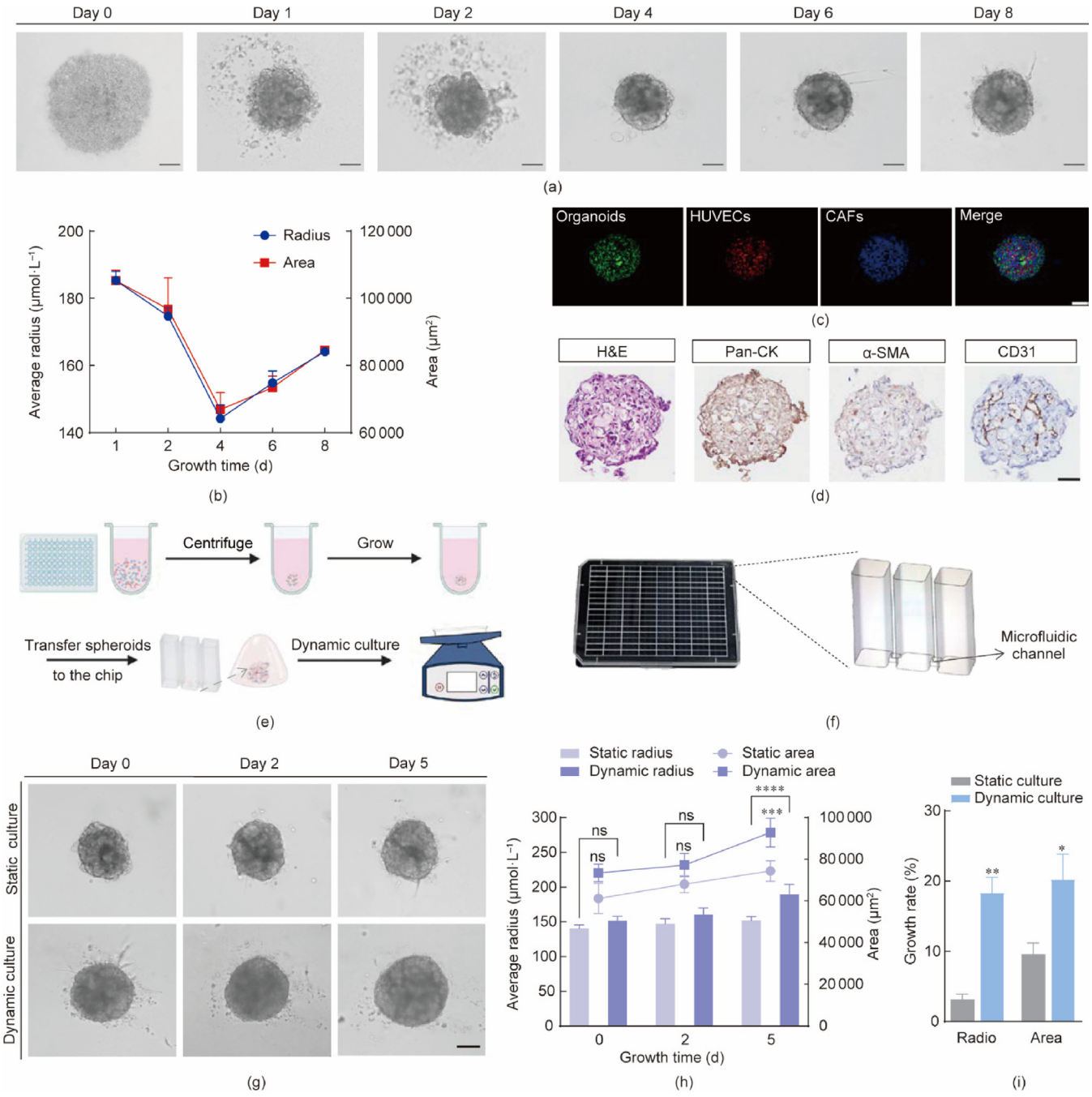

Fig. 3. Construction and characterization of ovarian cancer spheroid model. (a) Formation of ovarian cancer spheroids. Scale bars: 100 μm. (b) Growth curve of ovarian cancer spheroids. (c) Cell tracker of ovarian cancer spheroid. Scale bar: 200 μm. (d) H&E staining and immunohistochemical staining of ovarian cancer spheroid. Scale bar: 50 μm. (e) Construction method of ovarian cancer spheroid model. (f) Structure diagram and physical diagram of high-throughput microfluidic chips. (g) Static and dynamic culture of ovarian cancer spheroids in the chip. Scale bar: 50 μm. (h) Growth of ovarian spheroids in dynamic and static culture in the chip. (i) Growth rates of spheroid radius and surface area after 5 d under static versus dynamic culture conditions. Differences were analyzed using *t* tests to detect differences between groups of samples, $n = 3$. $^{*}p < 0.05$, $^{**}p < 0.01$, $^{***}p < 0.001$, $^{****}p < 0.0001$, ns: no statistically significant differences. Pan-CK: Pan cytokeratin.

dant perimeter elevation (indicating early-stage invasiveness) followed by sharp decline and stabilization (implying late-stage reduction).

3.5. Drug sensitivity testing in multiple in vitro models of ovarian cancer

We established multiple *in vitro* ovarian cancer models for drug sensitivity assessment. Preliminary evaluation of eight chemotherapeutic agents on organoids of two pathological types revealed pathological type-dependent sensitivity variations at identical drug concentrations via drug response curves (Fig. 5(a)). Substantial inter-patient half-maximal inhibitory concentration (IC50) variability (spanning several orders of magnitude) was observed for paclitaxel, carboplatin, cisplatin, gemcitabine, and docetaxel (Fig. 5(b)).

Additionally, we evaluated the therapeutic effects of four clinically common drug regimens on ovarian cancer spheroids. As illustrated in Fig. 5(c), the red fluorescence intensity in drug-treated groups was markedly higher than in the neutral control, indicating

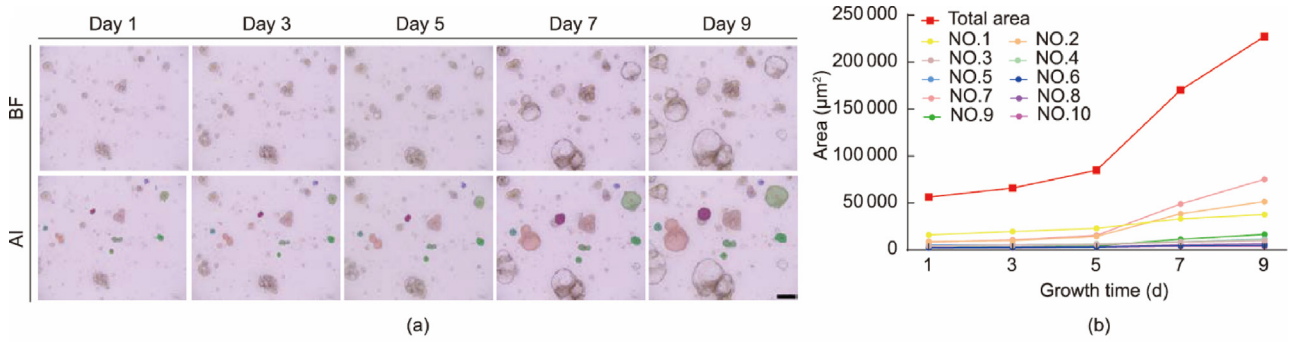

(a) (b)

Time	Total area (μm²)	Total perimeter (μm)	Total diameter (μm)	Average roundness	Average width height ratio	Average opacity	Total EPI
Day 1	56 203.11	2 835.58	1 463	0.816	1.028	0.739	1.16
Day 3	65 853.39	3 054.67	1 573	0.807	1.045	0.719	1.21
Day 5	84 793.28	3 410.17	1 766	0.820	0.993	0.715	1.07
Day 7	170 201.34	4 574.72	2 332	0.858	1.063	0.681	0.83
Day 9	227 331.11	5 135.92	2 575	0.874	1.053	0.694	0.72

(c)

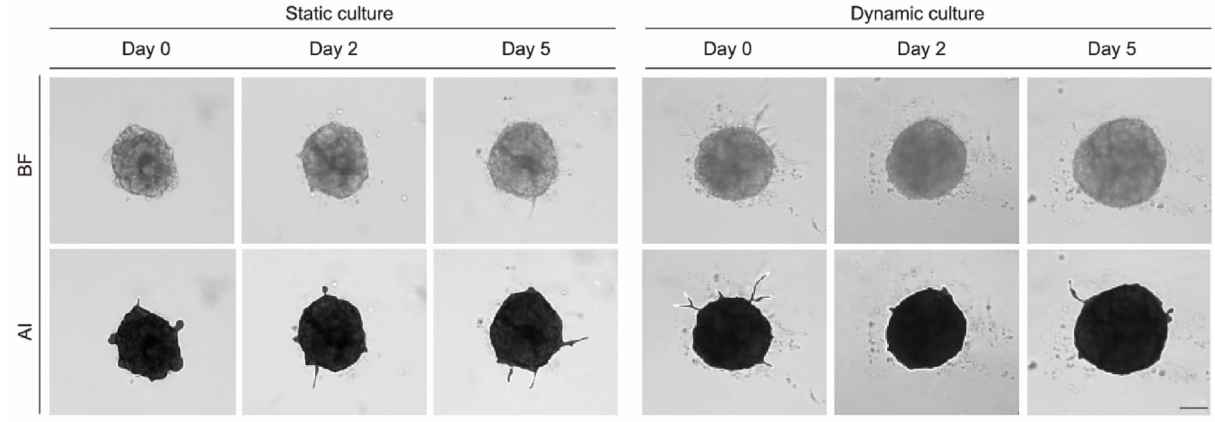

(d)

Time	Area (μm²)	Perimeter (μm)	Radius (μm)	Roundness	Width height ratio	Opacity	EPI
Static culture							
Day 0	54 299.68	932.97	136.25	0.784	0.93	0.50	0.33
Day 2	63 561.02	964.02	139.58	0.859	0.74	0.52	0.42
Day 5	68 708.13	1 001.82	146.06	0.860	0.98	0.55	0.64
Dynamic culture							
Day 0	70 333.78	1 018.69	148.575	0.852	1.01	0.53	0.99
Day 2	74 734.37	1 040.24	155.360	0.868	0.96	0.42	0.14
Day 5	95 199.29	1 177.48	176.940	0.863	1.09	0.54	0.36

(e)

Fig. 4. High-content analysis of ovarian cancer organoids and spheroids. (a) High-content analysis of organoids. Scale bar: 100 μm. (b) Organoid's growth rate. (c) High-content analysis parameters of organoids. (d) High-content analysis of intra-chip spheroids. Scale bar: 50 μm. (e) High-content analysis parameters of intra-chip spheroids. BF: bright field.

substantial spheroid killing efficacy. Notably, despite potent cytotoxicity across all regimens, paclitaxel and carboplatin combination therapy failed to yield significantly enhanced efficacy over monotherapies.

Evaluation across three models (organoid, spheroid-static, and spheroid-dynamic; Fig. 5(d)) showed robust growth in control organoids versus minimal size increase with darkening/disintegration in drug-treated organoids (indicating severely compromised viability). Analogous spheroid trends were observed: stable control growth versus near-complete growth arrest accompanied by cellular escape and diffuse distribution (Fig. S2 in Appendix A).

Fig. 5(e) highlights model-dependent divergence in drug treatment efficacy. Among spheroid models, drug efficacy was significantly higher in the dynamic versus static configuration. This discrepancy may reflect culture method-induced alterations in cellular growth dynamics and drug responsiveness.

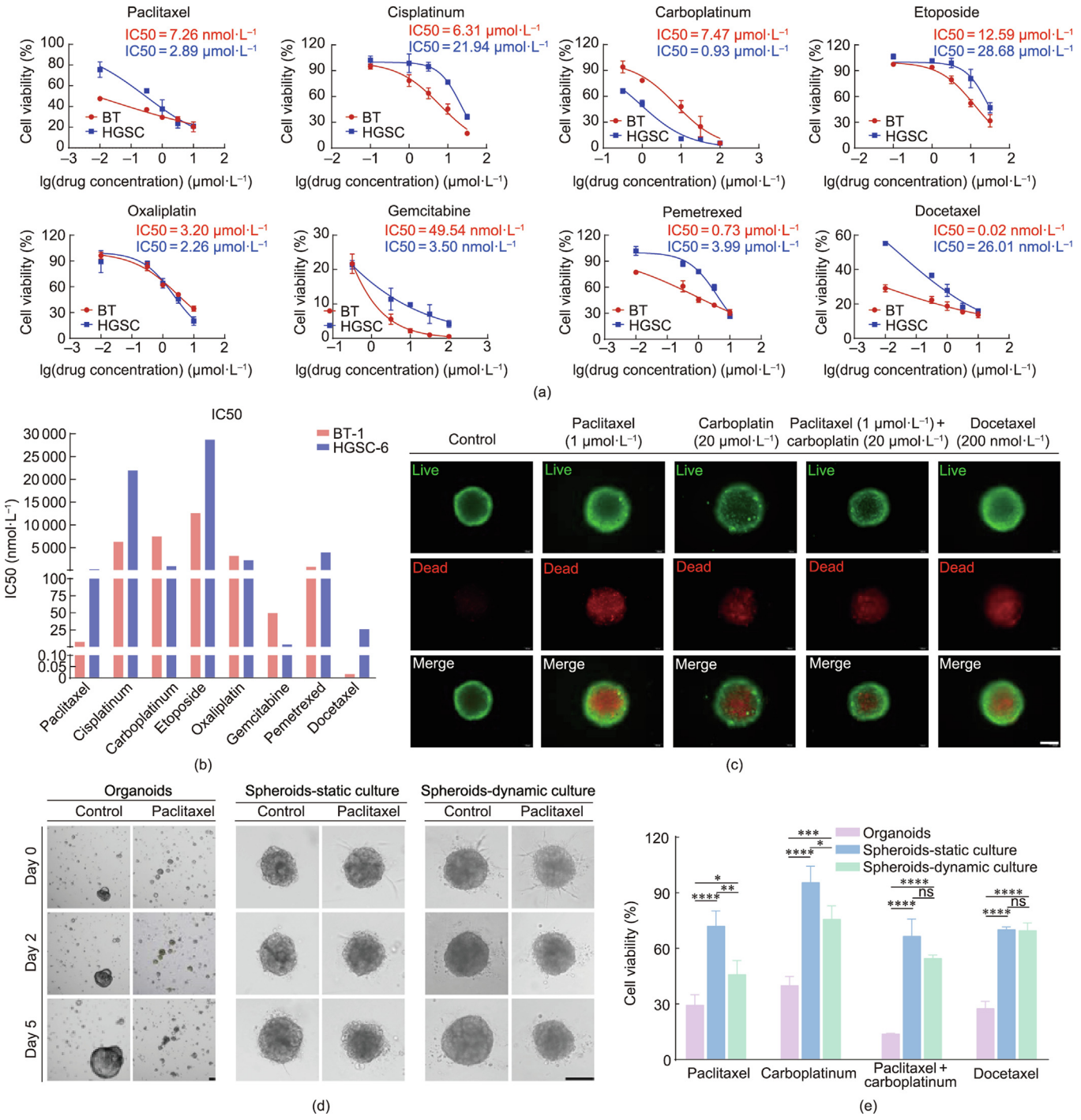

Fig. 5. Antimicrobial susceptibility testing of multiple ovarian cancer models. (a) Eight drug response curves of two organoids. (b) IC50 of eight drugs for two organoids. (c) Live/dead staining of spheroids after different drug effects. Scale bar: 200 μm. (d) Brightfield plots of single-concentration antimicrobial susceptibility tests of three ovarian cancer models. Scale bar: 100 μm. (e) Cell survival rate after single concentration drug action in three ovarian cancer models. Differences were analyzed using two-way analysis of variance (ANOVA) to detect differences between groups of samples, $n = 3$. $^{*}p < 0.05$, $^{**}p < 0.01$, $^{***}p < 0.001$, $^{****}p < 0.0001$, ns: no statistically significant differences.

3.6. Evaluation of CAR-MSLN-T therapy in ovarian cancer models

We constructed a multicellular *in vitro* ovarian cancer model using a plug-in membrane microfluidic chip to evaluate the efficacy of CAR-T therapy.

The multicellular model was established through sequential seeding of vascular endothelial cells, ovarian CAFs, and tumor spheroids (Fig. 6(a)) to create a biomimetic microenvironment. Fig. 6(b) displays the structural and physical diagrams of plug-in microfluidic chips, featuring a six-unit tripartite interconnected structure with a central chamber equipped with Transwell inserts for modular assembly. Following 24 h static and 48 h dynamic perfusion culture, progressive fusion between tumor spheroids and the CAFs layer was observed (Fig. 6(c)).

MSLN immunofluorescence staining confirmed high MSLN expression in multicellular spheroids (Fig. 6(d)). Figs. 6(e) and (f) evaluate CAR-MSLN-T cells in this model, showing time-dependent intensification of apoptotic fluorescence signals. While

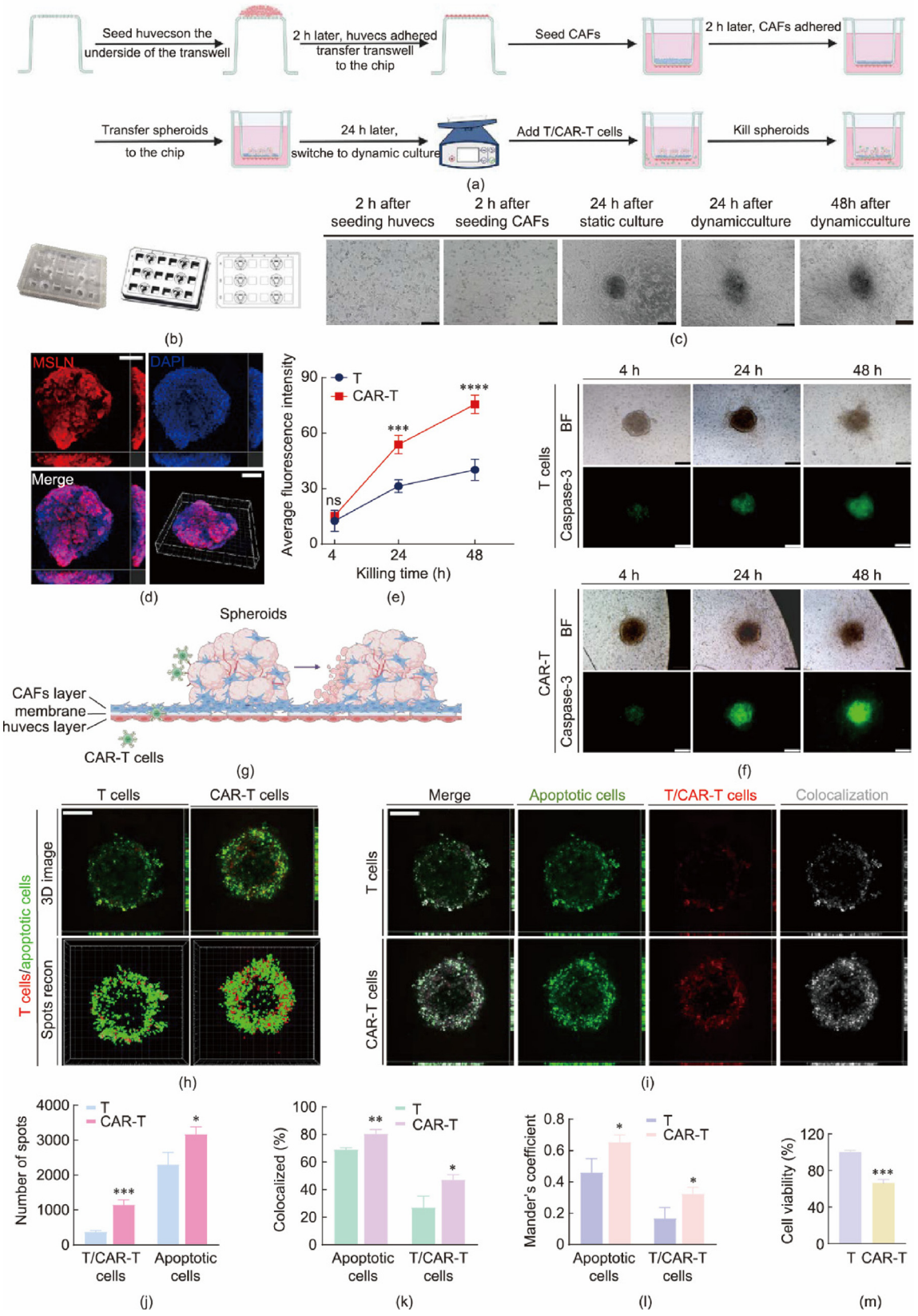

Fig. 6. Evaluation of CAR-T therapy in ovarian cancer spheroids. (a) Construction process of multicellular ovarian cancer model. (b) Plug-in chip structure diagram and physical drawing. (c) Brightfield diagram of cell seeding in multicellular ovarian cancer model. Scale bars: 200 μm. (d) MSLN immunofluorescence staining of ovarian cancer spheroids. Scale bars: 100 μm. (e) Average fluorescence intensity of caspase 3 at 4, 24, and 48 h of killing. (f) T/CAR-T killing effect at 4, 24, and 48 h (green staining indicates apoptotic cells). Scale bars: 200 μm. (g) Schematic diagram of CAR-T killing. (h) 3D fluorescence imaging and spots reconstruction of T/CAR-T-mediated spheroid killing at 24 h. Scale bar: 100 μm. (i) Colocalization analysis between T/CAR-T cells and apoptotic cells. Scale bar: 100 μm. (j) Statistical quantification of T/CAR-T cells and apoptotic cells spots reconstruction. (k) Colocalized area ratio of T/CAR-T and apoptotic signals relative to self-total signal. (l) Mander's coefficients of T/CAR-T cells and apoptotic cells. (m) Cell viability of T/CAR-T cells killing spheroids after 48 h treatment. Differences were analyzed using unpaired *t* tests to detect differences between groups of samples, $n = 3$. $^{*}p < 0.05$, $^{**}p < 0.01$, $^{***}p < 0.001$, ns: no statistically significant differences.

no significant efficacy difference was observed at 4 h, CAR-MSLN-T cells exhibited markedly enhanced tumor-killing capacity from 24 to 48 h. Fig. 6(g) schematically illustrates CAR-T cells penetrating multicellular barriers to eliminate tumor spheroids, elucidating the mechanistic basis for therapeutic superiority.

Further analysis utilizing 3D imaging and spots reconstruction demonstrated significantly increased apoptotic cell counts and enhanced immune infiltration in CAR-T groups compared to T cell controls (Figs. 6(h)–(j)). Quantitative analysis of post-colocalization fluorescence images was performed to measure colocalization areas between T/CAR-T signals and apoptotic signals, along with calculating Mander's coefficients (M1 for T/CAR-T and M2 for apoptotic signals) to quantify signal overlap efficiency (Figs. 6(k)–(m)).

4. Discussion

Patient-derived organoids (PDOs) constitute 3D models generated from fresh tumor specimens using *in vitro* 3D culture systems [10]. These models faithfully replicate patient-specific tumor characteristics and serve as pivotal tools in precision medicine and drug screening due to their physiological relevance, cost-effectiveness, and rapid establishment [16,17]. This study utilized 23 ovarian cancer surgical samples from 19 patients to establish 15 organoid lines 65.2 % success rate (Table S2 in Appendix A). Five organoids were maintained in short-term culture (2–4 weeks), while ten organoids underwent long-term culture (more than one month, maximum six months). H&E, immunohistochemical, and genomic analyses confirmed that organoids retain core parental tumor features, including histoarchitecture, biomarker expression, genomic profiles, and heterogeneity [11–15,27]. These organoids accurately recapitulate patient-specific pathophysiology, offering robust tools for ovarian cancer investigation [16,17].

To better mimic tumor microenvironments, we developed multicellular ovarian cancer spheroids incorporating vascular components. All cells were human-derived: organoids and CAFs (Fig. S3 in Appendix A) originated directly from tumor specimens. CAFs drive tumor invasion, chemoresistance, and immunosuppression via secretion of extracellular matrix (ECM), growth factors, and pro-inflammatory mediators [34]. HUVECs formed endothelial networks simulating tumor angiogenesis, facilitating nutrient/oxygen transport and metastasis [35]. This strategy eliminates interspecies disparities, while enabling cells to actively construct 3D architectures via ECM secretion during self-assembly processes, thereby enhancing physiological relevance [36]. Prior studies demonstrate spheroids replicate hallmark features of solid tumors, including cell–cell/ECM interactions [37], enhanced drug resistance [38,39], cellular polarity [40], and nutrient gradients [41].

Matrigel supplementation enhanced ECM simulation [42], improving bioactive signaling and spheroid integrity via adhesion molecule-mediated interactions while extending culture longevity [42]. Days 0–2 featured cellular self-aggregation with reduced spheroid radius, circumference, and area, indicating microenvironment-driven reorganization (Figs. 3(a) and (b)). Upon reaching stable density, spheroids exhibited significant expansion and pseudopod-like projections, potentially associated with intra vascularization (Fig. 3(a)). Volume dynamics of tumor spheroids (Figs. 3(a) and (b)) suggest association with CAF-mediated ECM remodeling or secreted factors modulating cellular interactions/proliferation. This manifested initially as either volume reduction or density increase, while subsequent cellular proliferation and microenvironmental adaptation collectively promoted volumetric expansion [43,44]. Concurrently, early angiogenesis deficiency may induce cellular malnutrition, with later HUVEC proliferation enabling gradual formation of vascular-like structures. This transition reversed initial volume contraction to progressive expansion [45–47].

During drug testing across diverse models, we unexpectedly observed accelerated spheroid growth under dynamic versus static culture conditions, highlighting biophysical influences (Figs. 3(g)–(i)). High-content analysis quantified spheroid growth parameters, revealing 15.16 % and 10.91 % increases in mean radius and surface area respectively in dynamic cultures compared to static controls after 5 d. This analysis indicated early-high-then-decreasing invasiveness in dynamic cultures versus progressive invasiveness enhancement in static systems (Figs. 4(d) and (e)), potentially attributable to size-dependent nutrient/oxygen limitations [41]. Prolonged culture may further elucidate this phenomenon. Collectively, organoid–CAF–HUVEC spheroids histologically and histochemically resemble ovarian carcinoma tissues, serving as valuable *in vitro* models (Fig. 3(d)). These spheroids exhibit superior cellular provenance and diversity compared to prior models by Joy et al. [20] and Dadgar et al. [23].

Drug sensitivity testing revealed organoid-specific chemotherapeutic responses across pathological subtypes, reflecting tumor heterogeneity. Therapeutic efficacy varied significantly among models (Fig. 5) [27,48,49]. Dynamic systems outperformed static models in drug responsiveness, where absent fluid shear stress may cause inadequate drug penetration and necrotic cores. Microfluidic perfusion sustains drug gradients, activates mechanotransduction pathways, and enhances tumor cell clearance, better simulating clinical responses [50].

This study presents rare chip-based evaluation of CAR-T potential against ovarian carcinoma [50,51], and constitutes the first tumor-on-chip assessment of MSLN-targeted CAR-T efficacy. CAR-T therapy, primarily used in hematologic malignancies, shows promise for ovarian carcinoma. MSLN—overexpressed in malignancies (e.g., ovarian/pancreatic cancers) but minimally in normal tissues [52,53]—represents a validated therapeutic target [54], with preclinical studies confirming CAR-MSLN-T safety/efficacy [55–57]. CAR-T evaluation experiments utilized organoids exhibiting significantly elevated MSLN expression (transcripts per million (TPM): 417.34) compared to normal ovarian tissue (median TPM: 0.43), while closely approximating ovarian tumor MSLN levels (median TPM: 428.73) (mRNA-seq data not depicted graphically) [58].

CAR-MSLN-T evaluation via image-based spots reconstruction, viability assays, and apoptotic fluorescence intensity confirmed superior tumoricidal activity versus T-cell controls (Figs. 6(e), (f), and (h)–(m)). Co-localization analysis revealed a spatial correlation exceeding 80 % between apoptotic regions and CAR-T cells, with this value being significantly higher than control levels (Fig. 6(k)). Furthermore, Mander's coefficients confirmed CAR-MSLN-T-dependent specific cytotoxicity (Fig. 6(l)), though notably only approximately 50 % of infused CAR-T cells participated in direct tumor killing, suggesting substantial potential for therapeutic optimization. Critically aberrant endothelial barriers and stromal microenvironments in solid tumors constitute primary obstacles for both immune effector cells and CAR-T therapy [59]. Specifically, TNF-α enhances T-cell tumor infiltration through multifaceted mechanisms: endothelial cell activation, vascular barrier integrity disruption, and intercellular gap expansion [60,61]. Consequently, numerous studies combine TNF-α with targeted therapeutic agents aiming to synergistically enhance CAR-T efficacy [62]. In contrast to Joy et al.'s CAR-T assessment model employing immortalized cell lines [20], our study innovatively utilizes PDOs for model construction. Importantly, the cellular composition proportions strictly reflect ovarian carcinoma single-cell sequencing data characteristics [24], thereby demonstrating inherent advantages in cellular provenance.

Future research must prioritize establishing integrated microvascular networks while concurrently developing physiologically relevant hypoxic gradients spanning tumor-stroma interfaces to recapitulate authentic immunosuppressive tumor microenvironments [63]. This foundational approach should be extended by implementing a multiplexed evaluation system that comprehensively integrates spatial transcriptomics, microfluidics-based drug screening, and AI-enabled resistance prediction [64]. Such integration will facilitate the development of anatomically faithful *in vitro* models and robust evaluative platforms, culminating in precision-driven therapeutic evolution.

5. Conclusions

In this study, we successfully generated 15 PDOs representing diverse histological subtypes from 23 surgical specimens of 19 patients, 15 PDOs representing diverse histological subtypes were generated. Morphological, immunohistochemical, and genomic analyses confirmed high concordance between organoids and parental tumors.

We further developed innovative vascularized multicellular spheroids by incorporating ovarian cancer organoids. Building on the successful construction of organoids and spheroids, both ovarian cancer spheroid models and multicellular models were established within microfluidic platforms, thereby extending the scope of this research. These models faithfully recapitulated tumor heterogeneity and microenvironmental complexity while providing dynamic flow-responsive culture conditions. Using these multi-model platforms, conventional chemotherapeutics and emerging CAR-MSLN-T immunotherapies were comparatively assessed, yielding novel therapeutic strategies and translational tools.

Future optimization strategies should surpass conventional *in vitro* model requirements—including integration of additional cellular components, hypoxic gradient simulation, and tumor microvasculature reconstruction—while prioritizing the reconstitution of ovarian cancer-specific pathological features. These critical features encompass the ascites-derived microenvironment and distinct metastasis patterns deviating from hematogenous/lymphatic dissemination observed in other malignancies. Such targeted reconstruction will maximize *in vitro* recapitulation of ovarian cancer microenvironments, thereby substantially enhancing biomimetic fidelity. We envision these optimized bioengineered platforms will advance precision oncology and accelerate therapeutic discovery for ovarian cancer, ultimately enabling personalized drug screening platforms and mechanistic immunotherapy studies.

CRediT authorship contribution statement

Jiexian Ye: Writing – original draft, Project administration, Formal analysis, Data curation, Conceptualization. **Hao Lin:** Supervision, Resources, Funding acquisition. **Zilin Zhang:** Formal analysis, Data curation. **Shihui Xu:** Project administration, Methodology, Data curation. **Feili Yang:** Project administration, Methodology. **Xuemei Zhuansun:** Project administration, Methodology, Data curation. **Feng Ji:** Resources. **Yusha Zhang:** Formal analysis, Data curation. **Yuxin Zhu:** Formal analysis, Data curation. **Jing Zhang:** Supervision, Project administration. **Zaozao Chen:** Writing – review & editing, Writing – original draft, Supervision, Funding acquisition, Conceptualization. **Zhongze Gu:** Writing – review & editing, Resources, Conceptualization. **Yang Shen:** Writing – review & editing, Resources, Funding acquisition, Conceptualization.

Declaration of competing interest

The authors declare that they have no known competing financial interests or personal relationships that could have appeared to influence the work reported in this paper.

Acknowledgments

This study is supported by the Science and Technology Project of Jiangsu Province (BK20232023 and BK20222008) and the National Key Research and Development Program of China (2017YFA0700500) to Zaozao Chen; the Noncommunicable Chronic Diseases-National Science and Technology Major Project (2025ZD0545600), the Zhongda Hospital Affiliated to Southeast University, Jiangsu Province High-Level Hospital Pairing Assistance Construction Fund (xdyyxy07), the Zhongda Hospital Affiliated to Southeast University, Jiangsu Province High-Level Hospital (2023GSPKY11), the National Clinical Key Discipline Construction Fund (gynecology czxm-zk-40), and the National Natural Science Foundation of China (82372126) to Yang Shen; the China Postdoctoral Science Foundation (2024M750460), the Nanjing Postdoctoral Research Foundation Project (FTJ-bh-2), the Zhongda Hospital Affiliated to Southeast University, Jiangsu Province High-Level Hospital Pairing Assistance Construction Fund (zdyyxy35), and the Fundamental Research Funds for the Central Universities (2242025K30022) to Hao Lin.

We are grateful to the staff in the Biobank of Zhongda Hospital Affiliated to Southeast University for technical assistance.

Appendix A. Supplementary data

Supplementary data to this article can be found online at https://doi.org/10.1016/j.eng.2025.08.028.

References

[1] Torre LA, Islami F, Siegel RL, Ward EM, Jemal A. Global cancer in women: burden and trends. Cancer Epidemiol Biomarkers Prev 2017;26(4):444–57.
[2] Jiang X, Tang H, Chen T. Epidemiology of gynecologic cancers in China. J Gynecol Oncol 2018;29(1):e7.
[3] Tanyi JL, Haas AR, Beatty GL, Stashwick CJ, O'Hara MH, Morgan MA, et al. Anti-mesothelin chimeric antigen receptor T cells in patients with epithelial ovarian cancer. J Clin Oncol 2016;34(15_suppl):5511.
[4] Maru Y, Hippo Y. Current status of patient-derived ovarian cancer models. Cells 2019;8(5):505.
[5] Lee WS, Kim HY, Seok JY, Jang HH, Park YH, Kim SY, et al. Genomic profiling of patient-derived colon cancer xenograft models. Medicine 2014;93(28):e298.
[6] Wu Q, Liu J, Wang X, Feng L, Wu J, Zhu X, et al. Organ-on-a-chip: recent breakthroughs and future prospects. Biomed Eng Online 2020;19(1):9.
[7] Stewart JM, Shaw PA, Gedye C, Bernardini MQ, Neel BG, Ailles LE. Phenotypic heterogeneity and instability of human ovarian tumor-initiating cells. Proc Natl Acad Sci 2011;108(16):6468–73.
[8] Dalerba P, Cho RW, Clarke MF. Cancer stem cells: models and concepts. Annu Rev Med 2007;58(1):267–84.
[9] Kryczek I, Liu S, Roh M, Vatan L, Szeliga W, Wei S, et al. Expression of aldehyde dehydrogenase and CD133 defines ovarian cancer stem cells. Int J Cancer 2012;130(1):29–39.
[10] Drost J, Clevers H. Organoids in cancer research. Nat Rev Cancer 2018;18(7):407–18.
[11] Sun H, Wang H, Wang X, Aoki Y, Wang X, Yang Y, et al. Aurora-A/SOX8/FOXK1 signaling axis promotes chemoresistance via suppression of cell senescence and induction of glucose metabolism in ovarian cancer organoids and cells. Theranostics 2020;10(15):6928–45.
[12] Maru Y, Tanaka N, Itami M, Hippo Y. Efficient use of patient-derived organoids as a preclinical model for gynecologic tumors. Gynecol Oncol 2019;154(1):189–98.
[13] Phan N, Hong JJ, Tofig B, Mapua M, Elashoff D, Moatamed NA, et al. A simple high-throughput approach identifies actionable drug sensitivities in patient-derived tumor organoids. Commun Biol 2019;2(1):1–11.
[14] Pauli C, Hopkins BD, Prandi D, Shaw R, Fedrizzi T, Sboner A, et al. Personalized *in vitro* and *in vivo* cancer models to guide precision medicine. Cancer Discov 2017;7(5):462–77.
[15] Tuveson D, Clevers H. Cancer modeling meets human organoid technology. Science 2019;364(6444):952–5.

[16] Aboulkheyr Es H, Montazeri L, Aref AR, Vosough M, Baharvand H. Personalized cancer medicine: an organoid approach. Trends Biotechnol 2018;36(4):358–71.
[17] Jin MZ, Han RR, Qiu GZ, Ju XC, Lou G, Jin WL. Organoids: an intermediate modeling platform in precision oncology. Cancer Lett 2018;414:174–80.
[18] Hill SJ, Decker B, Roberts EA, Horowitz NS, Muto MG, Worley Jr MJ, et al. Prediction of DNA repair inhibitor response in short-term patient-derived ovarian cancer organoids. Cancer Discov 2018;8(11):1404–21.
[19] Li S, Lei N, Chen M, Guo R, Han L, Qiu L, et al. Exploration of organoids in ovarian cancer: from basic research to clinical translation. Transl Oncol 2024;50:102130.
[20] Joy JD, Malacrida B, Laforêts F, Kotantaki P, Maniati E, Manchanda R, et al. Human 3D ovarian cancer models reveal malignant cell-intrinsic and -extrinsic factors that influence CAR T-cell activity. Cancer Res 2024;84(15):2432–49.
[21] Lal-Nag M, McGee L, Guha R, Lengyel E, Kenny HA, Ferrer M. A high-throughput screening model of the tumor microenvironment for ovarian cancer cell growth. SLAS Discov 2017;22(5):494–506.
[22] Ibrahim LI, Hajal C, Offeddu GS, Gillrie MR, Kamm RD. Omentum-on-a-chip: a multicellular, vascularized microfluidic model of the human peritoneum for the study of ovarian cancer metastases. Biomaterials 2022;288:121728.
[23] Dadgar N, Gonzalez-Suarez AM, Fattahi P, Hou X, Weroha JS, Gaspar-Maia A, et al. A microfluidic platform for cultivating ovarian cancer spheroids and testing their responses to chemotherapies. Microsyst Nanoeng 2020;6(1):1–12.
[24] Hietanen S, Oikkonen J, Hynninen J, Virtanen A, Häkkinen A, Hautaniemi S, et al. Longitudinal single-cell RNA-seq analysis reveals stress-promoted chemoresistance in metastatic ovarian cancer. Sci Adv 2022;8(8):eabm1831.
[25] Rajasekar S, Lin DSY, Abdul L, Liu A, Sotra A, Zhang F, et al. IFlowPlate-a customized 384-well plate for the culture of perfusable vascularized colon organoids. Adv Mater 2020;32(46):e2002974.
[26] Maenhoudt N, Defraye C, Boretto M, Jan Z, Heremans R, Boeckx B, et al. Developing organoids from ovarian cancer as experimental and preclinical models. Stem Cell Rep 2020;14(4):717–29.
[27] Kopper O, de Witte CJ, Lõhmussaar K, Valle-Inclan JE, Hami N, Kester L, et al. An organoid platform for ovarian cancer captures intra- and interpatient heterogeneity. Nat Med 2019;25(5):27.
[28] Lõhmussaar K, Kopper O, Korving J, Begthel H, Vreuls CPH, Van Es JH, et al. Assessing the origin of high-grade serous ovarian cancer using CRISPR-modification of mouse organoids. Nat Commun 2020;11(1):2660.
[29] Senkowski W, Gall-Mas L, Falco MM, Li Y, Lavikka K, Kriegbaum MC, et al. A platform for efficient establishment and drug-response profiling of high-grade serous ovarian cancer organoids. Dev Cell 2023;58(12):1106–1121.e7.
[30] Mayr D, Hirschmann A, Löhrs U, Diebold J. KRAS and BRAF mutations in ovarian tumors: a comprehensive study of invasive carcinomas, borderline tumors and extraovarian implants. Gynecol Oncol 2006;103(3):883–7.
[31] T CGA Research Network. Integrated genomic analyses of ovarian carcinoma. Nature 2011;474(7353):609–15.
[32] Adamson AW, Ding YC, Steele L, Leong LA, Morgan R, Wakabayashi MT, et al. Genomic analyses of germline and somatic variation in high-grade serous ovarian cancer. J Ovarian Res 2023;16(1):141.
[33] Chen Z, Ma N, Sun X, Li Q, Zeng Y, Chen F, et al. Automated evaluation of tumor spheroid behavior in 3D culture using deep learning-based recognition. Biomaterials 2021;272:120770.
[34] Gengenbacher N, Singhal M, Augustin HG. Preclinical mouse solid tumour models: status quo, challenges and perspectives. Nat Rev Cancer 2017;17(12):751–65.
[35] Zhang F, Zhu Y, Chen J, Kuang W, Huang R, Duan F, et al. Efficient endothelial and smooth muscle cell differentiation from human pluripotent stem cells through a simplified insulin-free culture system. Biomaterials 2021;271:120713.
[36] Kamatar A, Gunay G, Acar H. Natural and synthetic biomaterials for engineering multicellular tumor spheroids. Polymers 2020;12(11):2506.
[37] Doyle AD, Yamada KM. Mechanosensing via cell-matrix adhesions in 3D microenvironments. Exp Cell Res 2016;343(1):60–6.
[38] Khawar IA, Park JK, Jung ES, Lee MA, Chang S, Kuh HJ. Three dimensional mixed-cell spheroids mimic stroma-mediated chemoresistance and invasive migration in hepatocellular carcinoma. Neoplasia 2018;20(8):800–12.
[39] Gunay G, Kirit HA, Kamatar A, Baghdasaryan O, Hamsici S, Acar H. The effects of size and shape of the ovarian cancer spheroids on the drug resistance and migration. Gynecol Oncol 2020;159(2):563–72.
[40] Rafehi S, Ramos Valdes Y, Bertrand M, McGee J, Préfontaine M, Sugimoto A, et al. TGFβ signaling regulates epithelial-mesenchymal plasticity in ovarian cancer ascites-derived spheroids. Endocr Relat Cancer 2016;23(3):147–59.
[41] Mehta G, Hsiao AY, Ingram M, Luker GD, Takayama S. Opportunities and challenges for use of tumor spheroids as models to test drug delivery and efficacy. J Control Release 2012;164(2):192–204.
[42] Vukicevic S, Kleinman HK, Luyten FP, Roberts AB, Roche NS, Reddi AH. Identification of multiple active growth factors in basement membrane matrigel suggests caution in interpretation of cellular activity related to extracellular matrix components. Exp Cell Res 1992;202(1):1–8.
[43] Maruhashi T, Sugiura D, Okazaki IM, Okazaki T. LAG-3: from molecular functions to clinical applications. J Immunother Cancer 2020;8(2):e001014.
[44] Mao X, Xu J, Wang W, Liang C, Hua J, Liu J, et al. Crosstalk between cancer-associated fibroblasts and immune cells in the tumor microenvironment: new findings and future perspectives. Mol Cancer 2021;20(1):131.
[45] Carmeliet P, Jain RK. Molecular mechanisms and clinical applications of angiogenesis. Nature 2011;473(7347):298–307.
[46] Ayala-Domínguez L, Olmedo-Nieva L, Muñoz-Bello JO, Contreras-Paredes A, Manzo-Merino J, Martínez-Ramírez I, et al. Mechanisms of vasculogenic mimicry in ovarian cancer. Front Oncol 2019;9:998.
[47] Liu ZL, Chen HH, Zheng LL, Sun LP, Shi L. Angiogenic signaling pathways and anti-angiogenic therapy for cancer. Signal Transduct Target Ther 2023;8(1):198.
[48] Liu HD, Xia BR, Jin MZ, Lou G. Organoid of ovarian cancer: genomic analysis and drug screening. Clin Transl Oncol 2020;22(8):1240–51.
[49] Bi J, Newtson AM, Zhang Y, Devor EJ, Samuelson MI, Thiel KW, et al. Successful patient-derived organoid culture of gynecologic cancers for disease modeling and drug sensitivity testing. Cancers 2021;13(12):2901.
[50] Mu N, Gu J, Huang T, Zhang C, Shu Z, Li M, et al. A novel NF-κB/YY1/microRNA-10a regulatory circuit in fibroblast-like synoviocytes regulates inflammation in rheumatoid arthritis. Sci Rep 2016;6:20059.
[51] Zhuang J, Zhang J, Wu M, Zhang Y. A dynamic 3D tumor spheroid chip enables more accurate nanomedicine uptake evaluation. Adv Sci 2019;6(22):1901462.
[52] Lv J, Li P. Mesothelin as a biomarker for targeted therapy. Biomark Res 2019;7(1):18.
[53] Hassan R, Thomas A, Alewine C, Le DT, Jaffee EM, Pastan I. Mesothelin immunotherapy for cancer: ready for prime time? J Clin Oncol 2016;34(34):4171–9.
[54] Zhao R, Cui Y, Zheng Y, Li S, Lv J, Wu Q, et al. Human hyaluronidase PH20 potentiates the antitumor activities of mesothelin-specific CAR-T cells against gastric cancer. Front Immunol 2021;12:660488.
[55] Zhang Q, Liu G, Liu J, Yang M, Fu J, Liu G, et al. The antitumor capacity of mesothelin-CAR-T cells in targeting solid tumors in mice. Mol Ther Oncolytics 2021;20:556–68.
[56] Klampatsa A, Dimou V, Albelda SM. Mesothelin-targeted CAR-T cell therapy for solid tumors. Expert Opin Biol Ther 2021;21(4):473–86.
[57] Molloy ME, Austin RJ, Lemon BD, Aaron WH, Ganti V, Jones A, et al. Preclinical characterization of HPN536, a trispecific, T-cell-activating protein construct for the treatment of mesothelin-expressing solid tumors. Clin Cancer Res 2021;27(5):1452–62.
[58] Tang Z, Li C, Kang B, Gao G, Li C, Zhang Z. GEPIA: a web server for cancer and normal gene expression profiling and interactive analyses. Nucleic Acids Res 2017;45(W1):W98–W.
[59] Bellone M, Calcinotto A. Ways to enhance lymphocyte trafficking into tumors and fitness of tumor infiltrating lymphocytes. Front Oncol 2013;3:231.
[60] Calcinotto A, Grioni M, Jachetti E, Curnis F, Mondino A, Parmiani G, et al. Targeting TNF-α to neoangiogenic vessels enhances lymphocyte infiltration in tumors and increases the therapeutic potential of immunotherapy. J Immunol 2012;1950(188):2687–94.
[61] Sumransub N, El Jurdi N, Chiraphapphaiboon W, Maakaron JE. Putting function back in dysfunction: endothelial diseases and current therapies in hematopoietic stem cell transplantation and cellular therapies. Blood Rev 2022;51:100883.
[62] Mercogliano MF, Bruni S, Mauro F, Elizalde PV, Schillaci R. Harnessing tumor necrosis factor alpha to achieve effective cancer immunotherapy. Cancers 2021;13(3):564.
[63] Zhang TQ, Lv QY, Jin WL. The cellular-centered view of hypoxia tumor microenvironment: molecular mechanisms and therapeutic interventions. Biochim Biophys Acta 2024;1879(5):189137.
[64] Jin MZ, Jin WL. The updated landscape of tumor microenvironment and drug repurposing. Signal Transduct Target Ther 2020;5(1):166.